Star-forming galaxies dominate the diffuse, isotropic γ-ray background: extended data

Matt A. Roth[1,*], **Mark R. Krumholz**[1,2], **Roland M. Crocker**[1], **and Silvia Celli**[3]

[1]Research School of Astronomy and Astrophysics, The Australian National University, Canberra, Australia

[2]ARC Centre of Excellence for All-Sky Astrophysics in Three Dimensions (ASTRO-3D), Canberra, Australia

[3]Dipartimento di Fisica dell'Università La Sapienza e INFN, P. le Aldo Moro 2, 00185 Rome, Italy

[*]matt.roth@anu.edu.au

ABSTRACT

1 Extended data tables

Table 1. Local galaxy data

Galaxy	d_L [Mpc]	$\log M_*$ [$M_\odot$]	R_e [kpc]	$\dot{M}_*$ [$M_\odot$ yr^{-1}]	h_g [pc]	σ_g [km s^{-1}]	$\log \Sigma_g$ [$M_\odot$ pc^{-2}]
Arp 220	80.9 [1]	10.63 [2]	3.4 [3]	267 [4]	75 [5]	100 [5]	4.0 [5]
NGC 253	3.56 [1]	10.4 [6]	3.87 [7]	4.68 [6] / 1.73 [8] [b]	130 [5]	26 [5]	2.6 [5]
M 31	0.77 [1]	10.84 [9]	1.38 [10]	0.40 [9]	150 [11]	10 [12]	0.68 [13]
NGC 4945	3.72 [1]	10.52 [14]	2.34 [15]	4.35 [16]	-[a]	20 [17]	-[a]

For each entry, we give a value followed by the reference from which that value is taken.

[a] NGC 4945 is observed edge-on, so measurements of the gas scale height and gas surface density are unavailable. We derive them in the usual manner, as described in the Methods, using the measured gas velocity dispersion.

[b] The gas data come exclusively from the nuclear starburst region, so we give two SFR estimates: the first is for the entire galaxy, and the second is for the nuclear starburst region only. We use the former for our stellar data spectrum prediction and the latter for our gas prediction.

2 Extended data figures

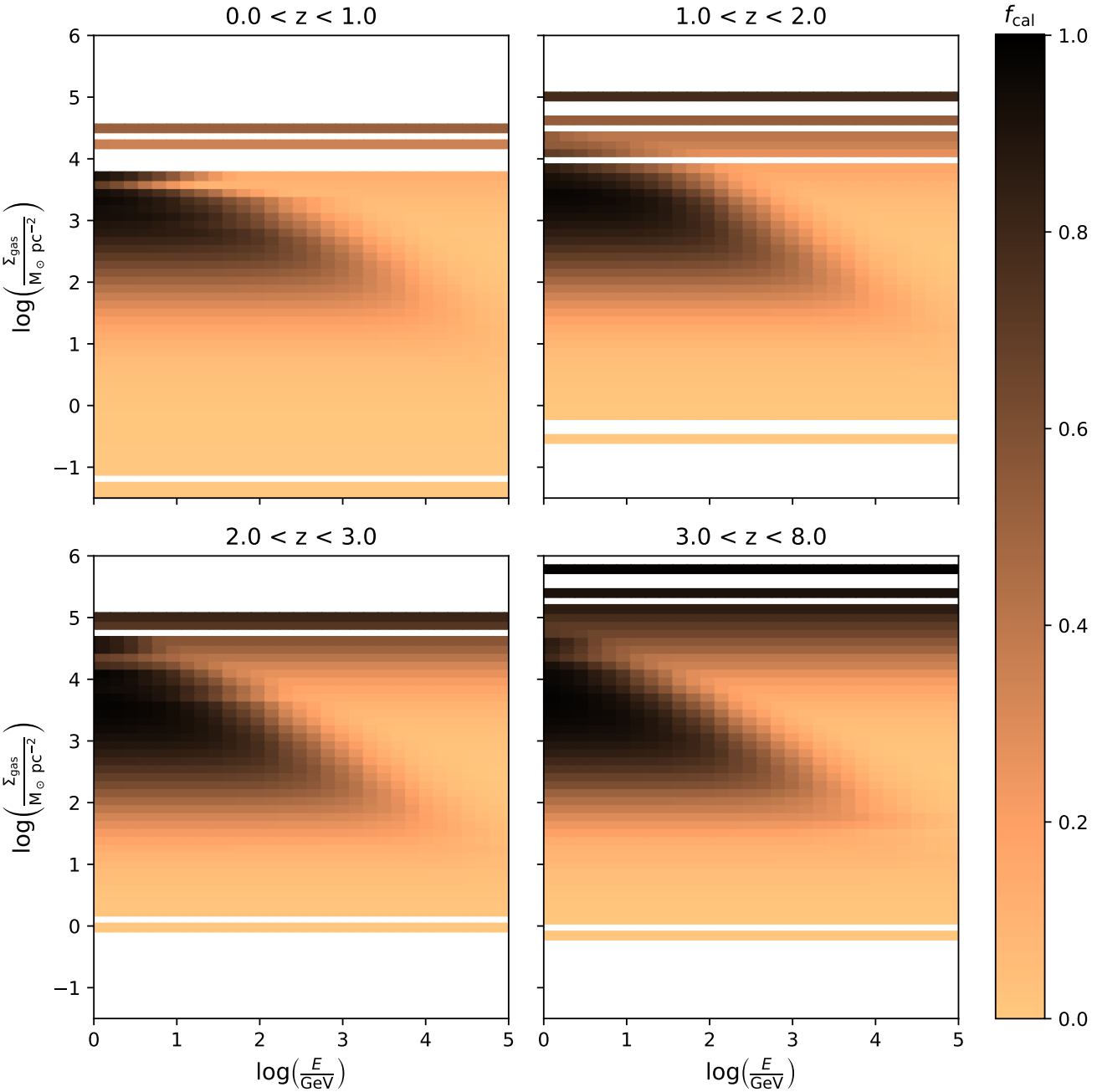

Figure 1. Mean calorimetry fraction $f_{\rm cal}(E)$ in the surface gas density Σ_g, cosmic ray energy E plane, binned in redshift intervals. This figure is constructed by deriving the gas surface density and energy dependent calorimetry fraction for each galaxy in the CANDELS sample using our model. The colour of each pixel gives the mean calorimetry fraction of all the galaxies within that particular range of Σ_g, E, and redshift. The horizontal white stripes correspond to ranges of Σ_g into which no CANDELS galaxies fall for the corresponding redshift range. Several physical processes contribute to the behaviour visible in the plot. At low Σ_g, galaxies have low $f_{\rm cal}$ at all energies E because there are few targets for hadronic collisions with CRs. As Σ_g increases, the increased ISM density results in efficient calorimetry and conversion of CR energy into γ-rays for low CR energies; however, at higher energies the CR number density is low, yielding a high CR streaming velocity and rapid escape, resulting in low $f_{\rm cal}$. As Σ_g increases further, the increasing density results in the streaming instability being suppressed efficiently by ion-neutral damping towards lower energies, reducing the calorimetry fraction further. Finally, at the highest Σ_g, the streaming instability is suppressed completely by ion-neutral damping, but streaming is still limited to the speed of light. Consequently, increasing Σ_g further only results in increased collisions, and thus a higher calorimetry fraction.

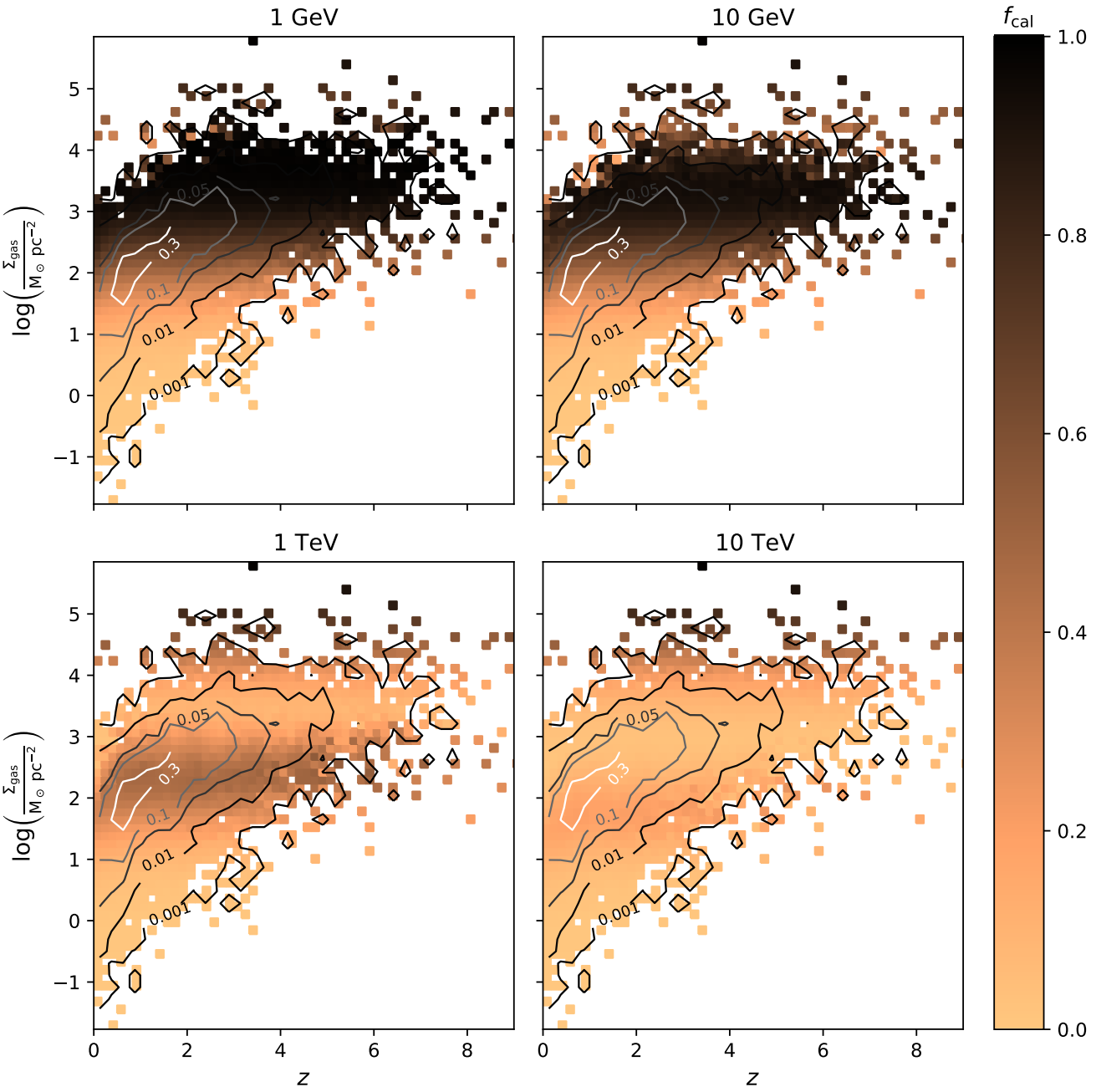

Figure 2. Calorimetry fraction in the surface gas density (Σ_g), redshift (z) plane at CR energies $E = 1$ GeV, 10 GeV, 1 TeV and 10 TeV. To construct this figure, for each CANDELS sample galaxy, we apply our model to compute Σ_g and $f_{\rm cal}(E)$ at the indicated energies. The colour indicates the average $f_{\rm cal}(E)$ value computed over bins of (z, Σ_g), while contours indicate the density of the CANDELS sample in this plane. Note that the non-monotonic behaviour of $f_{\rm cal}(E)$ with Σ_g that is most prominently visible in the 1 TeV panel is expected, for the reasons explained in the caption of Extended Data Figure 1.

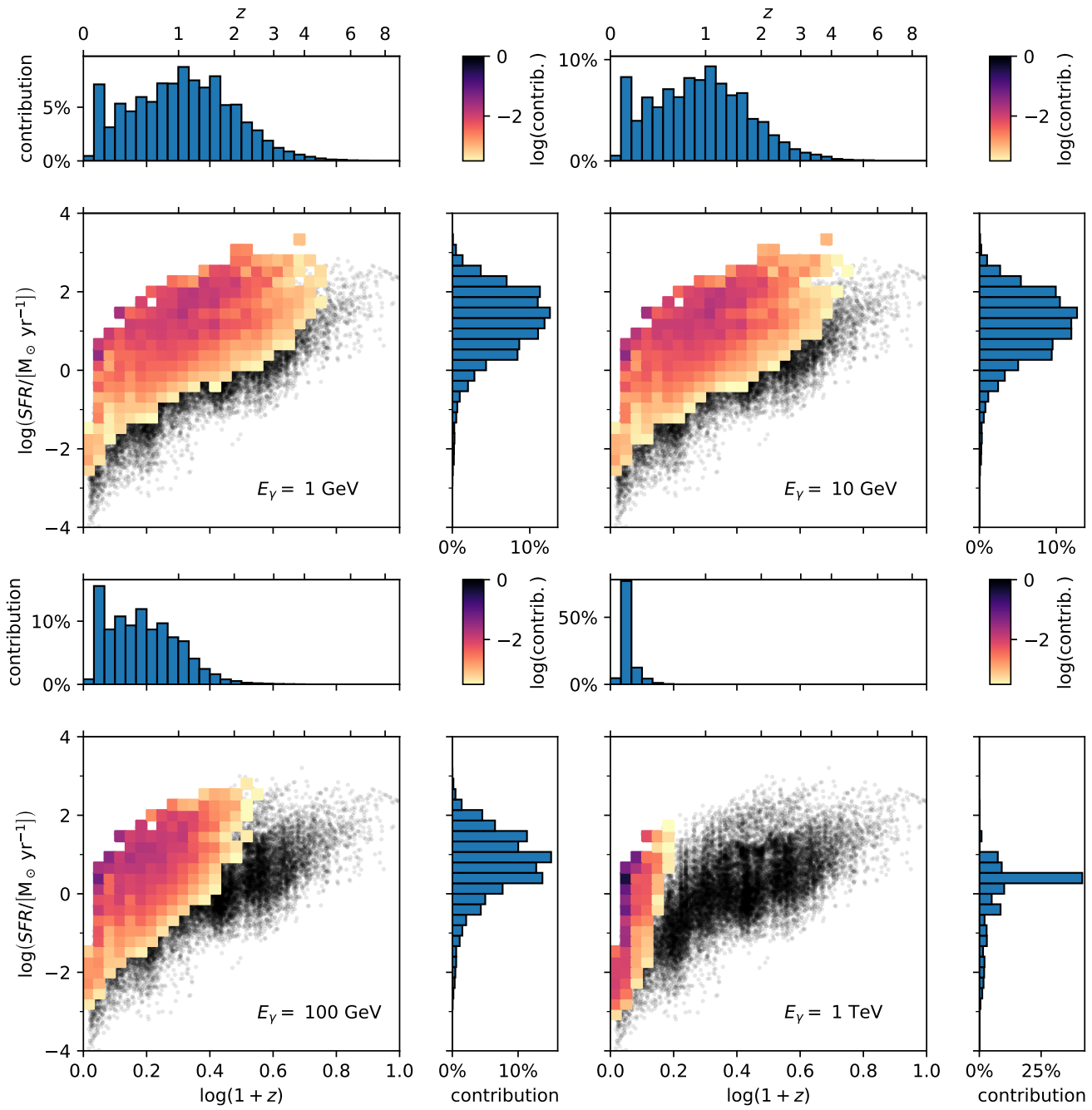

Figure 3. The contribution of SFGs to the total γ-ray spectrum at selected energies in the star formation rate ($\dot{M}_*$), redshift (z) plane. Coloured pixels show the fractional contribution (as indicated in the colourbar) from galaxies in each bin of $\dot{M}_*$ and z to the diffuse isotropic γ-ray background at the indicated energy; a fractional contribution of unity corresponds to that pixel producing all of the background, with no contribution from galaxies outside the pixel. Grey points show individual CANDELS galaxies in regions of $\dot{M}_*$ and z that contribute $< 10^{-3}$ of the total. Flanking histograms show the fractional contribution binned in one dimension – $\dot{M}_*$ (right) and z (top). We see that the background at lower energies is dominated by emission from galaxies on the high side of the star forming main sequence at $z \sim 1-2$, while at high energies it is dominated by the brightest systems at low redshift.

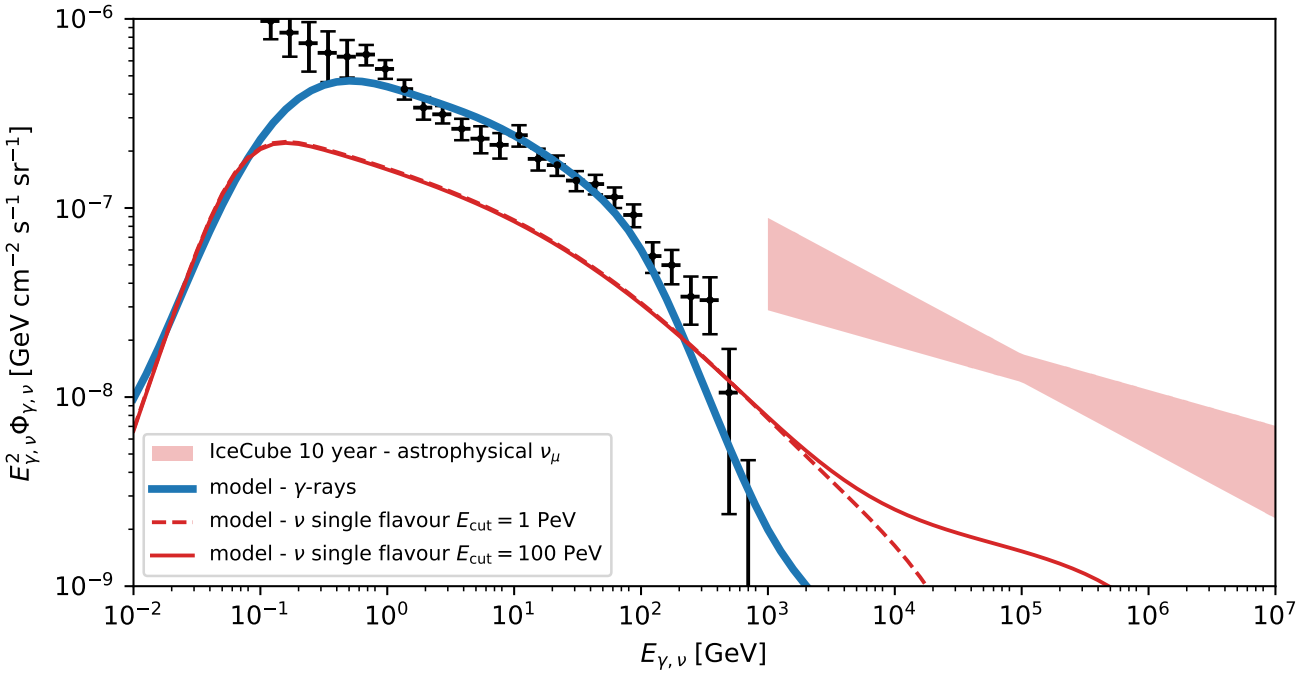

Figure 4. The diffuse γ-ray and neutrino backgrounds. The blue line and black points show the model-predicted and observed γ-ray background, and are identical to those shown in Figure 4. The red lines show our model prediction for the neutrino background (single flavour) with $E_{\rm cut} = 100$ PeV (solid line) and $E_{\rm cut} = 1$ PeV (dashed line), computed as described in the Supplementary Information. We assume a neutrino flavour ratio at the detector of $(\nu_e : \nu_\mu : \nu_\tau) = (1 : 1 : 1)$. The red filled band shows a power law fit [18] to the single flavour astrophysical neutrino background.

References

1. Kornecki, P. *et al.* γ-ray/infrared luminosity correlation of star-forming galaxies. **641,** A147. arXiv: 2007.07430 [astro-ph.HE] (Sept. 2020).
2. Rodrıguez Zaurın, J., Tadhunter, C. N. & González Delgado, R. M. Optical spectroscopy of Arp220: the star formation history of the closest ULIRG. **384,** 875–885. arXiv: 0711.0166 [astro-ph] (Mar. 2008).
3. Wright, G. S., James, P. A., Joseph, R. D., McLean, I. S. & Doyon, R. *Infrared images of merging galaxies.* in *NASA Conference Publication* (eds Sulentic, J. W., Keel, W. C. & Telesco, C. M.) **3098** (Nov. 1990), 321–326.
4. Torres, D. F. Theoretical Modeling of the Diffuse Emission of Gamma Rays from Extreme Regions of Star Formation: The Case of ARP 220. **617,** 966–986. arXiv: astro-ph/0407240 [astro-ph] (Dec. 2004).
5. Krumholz, M. R. *et al.* Cosmic ray transport in starburst galaxies. **493,** 2817–2833. arXiv: 1911.09774 [astro-ph.HE] (Apr. 2020).
6. Parkash, V., Brown, M. J. I., Jarrett, T. H. & Bonne, N. J. Relationships between HI Gas Mass, Stellar Mass, and the Star Formation Rate of HICAT+WISE (H I-WISE) Galaxies. **864,** 40. arXiv: 1807.06246 [astro-ph.GA] (Sept. 2018).
7. IRSA. *NASA/IPAC Infrared Science Archive* https://irsa.ipac.caltech.edu.
8. Bendo, G. J. *et al.* ALMA observations of 99 GHz free-free and H40α line emission from star formation in the centre of NGC 253. **450,** L80–L84. arXiv: 1504.02142 [astro-ph.GA] (June 2015).
9. Rahmani, S., Lianou, S. & Barmby, P. Star formation laws in the Andromeda galaxy: gas, stars, metals and the surface density of star formation. **456,** 4128–4144. arXiv: 1512.06675 [astro-ph.GA] (Mar. 2016).
10. Blaña Dıaz, M. *et al.* Sculpting Andromeda - made-to-measure models for M31's bar and composite bulge: dynamics, stellar and dark matter mass. **481,** 3210–3243. arXiv: 1808.07494 [astro-ph.GA] (Dec. 2018).
11. Braun, R. & Walterbos, R. A. M. Physical Properties of Neutral Gas in M31 and the Galaxy. **386,** 120 (Feb. 1992).
12. Caldú-Primo, A. & Schruba, A. Molecular Gas Velocity Dispersions in the Andromeda Galaxy. **151,** 34. arXiv: 1512.00479 [astro-ph.GA] (Feb. 2016).
13. Kennicutt Robert C., J. The Global Schmidt Law in Star-forming Galaxies. **498,** 541–552. arXiv: astro-ph/9712213 [astro-ph] (May 1998).
14. Davis, B. L., Graham, A. W. & Cameron, E. Black Hole Mass Scaling Relations for Spiral Galaxies. II. M_{BH}-$M_{*,tot}$ and M_{BH}-$M_{*,disk}$. **869,** 113. arXiv: 1810.04888 [astro-ph.GA] (Dec. 2018).
15. de Vaucouleurs, G. Southern Galaxies. V. Isophotometry of the Large Barred Spiral NGC 4945. **139,** 899 (Apr. 1964).
16. Bendo, G. J. *et al.* Free-free and H42α emission from the dusty starburst within NGC 4945 as observed by ALMA. **463,** 252–269. arXiv: 1607.02304 [astro-ph.GA] (Nov. 2016).

17. Ott, M., Whiteoak, J. B., Henkel, C. & Wielebinski, R. Atomic and molecular gas in the starburst galaxy NGC 4945. **372,** 463–476. arXiv: astro-ph/0109190 [astro-ph] (June 2001).

18. Stettner, J. *Measurement of the diffuse astrophysical muon-neutrino spectrum with ten years of IceCube data* in *36th International Cosmic Ray Conference (ICRC2019)* **36** (July 2019), 1017. arXiv: 1908.09551 [astro-ph.HE].